Title
Building-Block Size Mediates Microporous Annealed Particle Hydrogel Tube Microenvironment Following Spinal Cord Injury

Journal
Advanced Healthcare Materials, 13(25)

ISSN
2192-2640

Authors
Ross, Brian C
Kent, Robert N
Saunders, Michael N
et al.

Publication Date
2024-10-01

DOI
10.1002/adhm.202302498

ADVANCED HEALTHCARE MATERIALS
www.advhealthmat.de

Building-Block Size Mediates Microporous Annealed Particle Hydrogel Tube Microenvironment Following Spinal Cord Injury

*Brian C. Ross, Robert N. Kent III, Michael N. Saunders, Samantha R. Schwartz, Brooke M. Smiley, Sarah E. Hocevar, Shao-Chi Chen, Chengchuan Xiao, Laura A. Williams, Aileen J. Anderson, Brian J. Cummings, Brendon M. Baker, and Lonnie D. Shea**

Spinal cord injury (SCI) is a life-altering event, which often results in loss of sensory and motor function below the level of trauma. Biomaterial therapies have been widely investigated in SCI to promote directional regeneration but are often limited by their pre-constructed size and shape. Herein, the design parameters of microporous annealed particles (MAPs) are investigated with tubular geometries that conform to the injury and direct axons across the defect to support functional recovery. MAP tubes prepared from 20-, 40-, and 60-micron polyethylene glycol (PEG) beads are generated and implanted in a T9-10 murine hemisection model of SCI. Tubes attenuate glial and fibrotic scarring, increase innate immune cell density, and reduce inflammatory phenotypes in a bead size-dependent manner. Tubes composed of 60-micron beads increase the cell density of the chronic macrophage response, while neutrophil infiltration and phenotypes do not deviate from those seen in controls. At 8 weeks postinjury, implantation of tubes composed of 60-micron beads results in enhanced locomotor function, robust axonal ingrowth, and remyelination through both lumens and the inter-tube space. Collectively, these studies demonstrate the importance of bead size in MAP construction and highlight PEG tubes as a biomaterial therapy to promote regeneration and functional recovery in SCI.

1. Introduction

Trauma to the spinal cord often results in permanent loss of sensory and motor function below the level of injury.[1] Damage results both from the initial injury and from a secondary inflammatory cascade in which immune cells rapidly infiltrate via the disrupted blood-spinal cord barrier. These cells, including activated macrophages and neutrophils, secrete inflammatory factors that exacerbate neuronal and oligodendrocyte cell death, axon loss, and demyelination, ultimately resulting in the formation of a fibrotic or necrotic defect.[1,2] Pro-inflammatory factors further induce the activation of astrocytes, which secrete a dense glial scar surrounding the lesion, creating a mechanical and chemical barrier through which axons of spared neurons cannot penetrate.[3–5] Beyond the glial scar, axons require support and guidance to cross the prohibitive environment within the defect.[6] In order to facilitate regeneration of lost tissue, therapies are needed that modulate the immune

B. C. Ross, R. N. Kent III, M. N. Saunders, S. R. Schwartz, B. M. Smiley, S. E. Hocevar, S.-C. Chen, L. A. Williams, B. M. Baker, L. D. Shea
Department of Biomedical Engineering
University of Michigan
2200 Bonisteel Blvd, Ann Arbor, MI 48109, USA
E-mail: ldshea@umich.edu

The ORCID identification number(s) for the author(s) of this article can be found under https://doi.org/10.1002/adhm.202302498

DOI: 10.1002/adhm.202302498

S. E. Hocevar, L. D. Shea
Neuroscience Graduate Program
University of Michigan Medical School
204 Washtenaw Ave, Ann Arbor, MI 48109, USA

C. Xiao
Department of Molecular
Cellular, and Developmental Biology
University of Michigan
1105 North University Ave, Ann Arbor, MI 48109, USA

A. J. Anderson, B. J. Cummings
Institute for Memory Impairments and Neurological Disorders
University of California
Biological Sciences III, 2642, Irvine, CA 92697, USA

A. J. Anderson, B. J. Cummings
Sue and Bill Gross Stem Cell Research Center
University of California
845 Health Sciences Rd, Irvine, CA 92697, USA

response, attenuate scarring, and support the growth of axons across the injury.

Biomaterials have widely been employed in the injured spinal cord to fill the tissue defect, stabilize injured tissue, support cell infiltration, and deliver therapeutic factors.[7] Bridges have been studied as a means of reducing scarring and providing directional guidance to regenerating axons. We have previously reported the use of porous multi-channel poly(lactide-co-glycolide) (PLG) bridges to stabilize the injury, support axonal regrowth and remyelination, and improve functional recovery.[8–12] The channels within the bridge direct cellular alignment and axon growth across the injury. Hydrogels have also been employed as therapies, as they more closely match the mechanical properties of the spinal cord and injectable formulations can readily conform to the geometry of the injury.[13,14] The benefits of both hydrogel materials and aligned axonal growth have been harnessed by creating tubes composed of microporous annealed particles (MAPs) that can be employed as modular bridges, with the number and length of tubes adapted at the time of implantation to stabilize injuries with unique geometries.[15–17] MAP gels reduce counts of reactive astrocytes in models of stroke, suggesting that they may attenuate glial scarring in spinal cord injury (SCI).[18] Further, MAPs promote complex vascular network integration, provide support for regenerating axons, and improve functional recovery. [17,19]

Herein, we investigate the design parameters for MAPs with tubular geometries as bridges for treating SCI that modulate the inflammatory response, attenuate scar formation, and provide support to guide regenerating axons across the injury. The plasticity of MAPs allows them to be easily formed into implants that provide both modularity and directional cues. Small, medium, and large polyethylene glycol (PEG) beads were produced using microfluidics, annealed into tubes, and subsequently inserted into a murine T9-10 hemisection model of SCI. Porosity, material properties, and off-the-shelf use, enabled by lyophilization, were investigated. MAPs of low-polydispersity microgels offer control over pore size and porosity, [20,21] which influence immune cell phenotypes and may attenuate secondary injury in SCI. [22,23] Macrophages adopt differential phenotypes dependent on spatial confinement generated by microgel size, indicating that the physical properties of MAPs may have bioactive effects.[20,21] Previous studies have investigated the effects of microgel size with diameters ranging from 40–145 micron, with indications that 40-micron beads may upregulate pro-regenerative macrophage markers.[20] As such, this study investigates hydrogel tubes composed of 20-, 40-, and 60- micron beads, which we hypothesize may modulate acute and chronic inflammatory responses that are driven largely by macrophages and microglia. The extent of glial and fibrotic scarring were assessed at a sub-acute timepoint. Regeneration through the injury was assessed by quantification of axons and myelination, as well as through functional recovery using the Basso Mouse Scale (BMS) and ladder beam walking task.[24,25] Together, the findings of this study demonstrate the design of modular hydrogel tubes as a promising therapy for SCI and highlight the importance of MAP building size for applications in traumatic central nervous system (CNS) injury.

A. J. Anderson, B. J. Cummings
Physical Medicine and Rehabilitation
University of California
18124 Culver Dr # F, Irvine, CA 92612, USA
B. M. Baker, L. D. Shea
Department of Chemical Engineering
University of Michigan
2300 Hayward St, Ann Arbor, MI 48109, USA

2. Results

2.1. Low-Polydispersity Hydrogel Building-Blocks Enable Control Over Porosity and Material Properties

PEG beads were produced by passing 8-arm PEG-maleimide and plasmin-sensitive YKND peptide[26] through water-in-oil microfluidic droplet generators,[27] with subsequent crosslinking carried out by Michael-type addition (Figure S1A, Supporting Information). Small, medium, and large beads (**Figure 1**A) were produced using microfluidic devices with 20-, 40-, and 60-micron ceiling heights. The resulting beads had average diameters of 20.8, 40.7, and 58.4 μm, respectively, closely matching microfluidic device sizes. All bead sizes had polydispersity indices less than or equal to 0.10, indicating successful generation of largely monodisperse populations (Figure 1B). Beads were lyophilized according to the microengineered emulsion-to-powder technique to maintain hydrogel structure and preserve pendant maleimide groups, which were utilized in annealing processes.[28]

Tubes were created by rehydrating lyophilized beads in a solution of photoinitiator, packing hydrated beads into capillaries with pins to create lumens, and annealing by exposure to ultraviolet light (Figure S1B, Supporting Information). The resulting hydrogel tubes had outer diameters of 400 microns with 250-micron lumens (Figure 1C). Tubes were then lyophilized and stored until use (Figure 1D). Tubes rehydrated following lyophilization maintained clear separation of granular beads and similar dimensions to tubes that had never been lyophilized (Figure 1E). Further, materials rehydrated from the lyophilized state showed no significant differences in compressive moduli, pore cross-sectional area, or void fraction compared to freshly prepared materials (Figure S3A–D, Supporting Information). Tubes of all compositions expanded in length by ~1.3x from the lyophilized state upon rehydration (Figure 1G). This property makes lyophilization particularly attractive, as tubes can be inserted into SCI and will subsequently expand to achieve tight apposition with the rostral and caudal sides of the injury as rehydration occurs. Compressive moduli were assessed using slabs composed of beads to avoid any confounding effects produced by complex tubular geometry. Moduli were found to be dependent on bead size, with moduli of 30.4, 84.1, and 191.0 kPa for slabs composed of 20-, 40-, and 60-micron beads, respectively (Figure 1H). The observed bead size-dependent increase in compressive modulus is likely an effect of the high-stiffness annealing solution used for material construction.[17,20,29,30] Although tissues of the central nervous system are generally anisotropic, all observed moduli were within the range of reported material properties for spinal cord tissue.[31–33]

The porosity of MAPs was assessed by confocal contrast imaging of Cy5-doped slabs in fluorescein isothiocyanate-dextran (FITC-dextran) solution (Figure 1F). The average pore cross-sectional area was found to be dependent on bead size, with larger

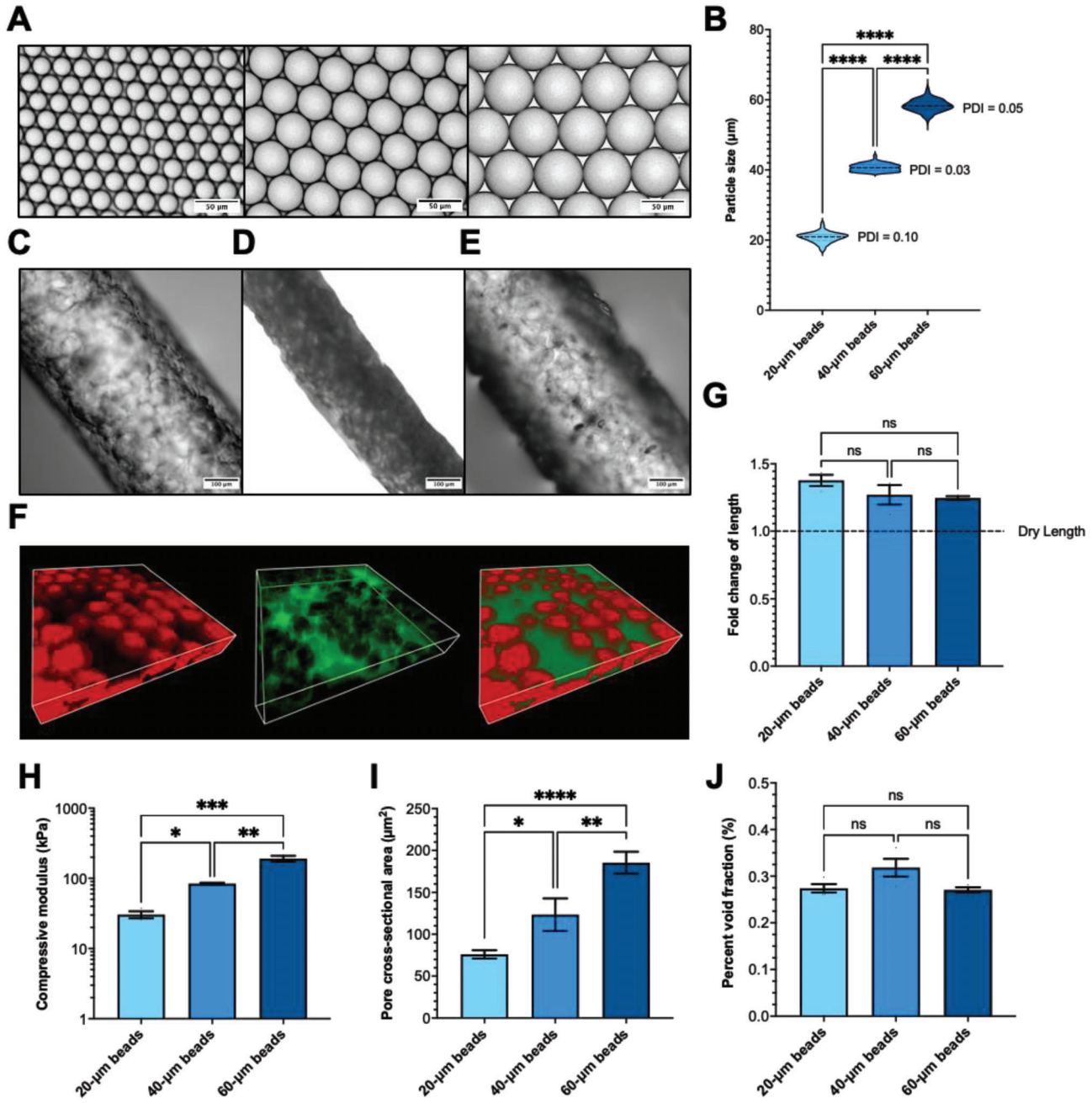

Figure 1. Properties of PEG tubes composed of low-polydispersity beads. A) Brightfield images of small, medium, and large beads produced using 20-, 40-, and 60-micron microfluidic devices. B) Particle size distributions for 20-, 40-, and 60-micron beads. Brightfield images of a C) pre-lyophilized tube, D) lyophilized tube, and E) rehydrated tube. F) Fluorescent confocal image of annealed Cy5 60-micron beads (red) in FITC-dextran (green). G) Fold change in length upon rehydration of tubes. H) Microsquisher-derived compressive moduli of slabs composed of 20-, 40-, and 60-micron beads. I) Average pore-cross sectional area and J) void fraction determined by confocal imaging. Statistical analysis: one-way ANOVA with Tukey's multiple comparisons test. $*p < 0.05$, $**p < 0.01$, $***p < 0.001$, and $****p < 0.0001$. Error bars: mean ± standard error of the mean; $n = 3$ samples per bead size.

beads resulting in larger pores. (Figure 1I). Despite the low polydispersity of the component beads, pores were widely variable in size, likely due to compression of the soft beads and imperfect packing.[34] Wall void fraction was found to be independent of bead size, although walls composed of 40-micron beads trended toward higher void fractions, likely due to their lower polydispersity relative to other bead sizes produced (Figure 1J).

2.2. Glial and Fibrotic Scarring are Attenuated by PEG Tubes

Previous reports have observed that MAPs reduce both fibrosis and gliosis, motivating our initial studies assessing the degree of scarring present at the injury. Animals were subjected to T9-10 hemisection injuries, and five individual tubes were inserted into the injury and allowed to swell to attain rostral and caudal

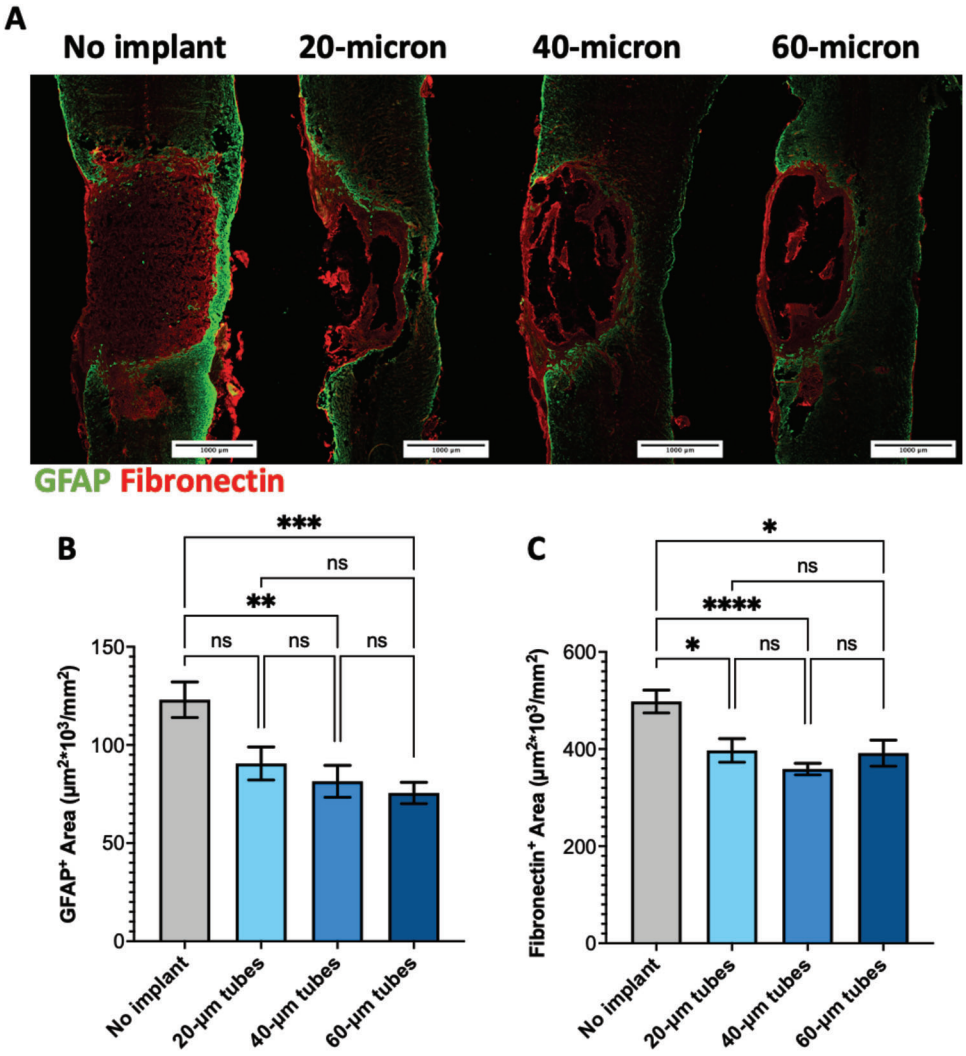

Figure 2. PEG tubes attenuate glial and fibrotic scarring. Animals were given T9-10 hemisection injuries and subsequently received tubes composed of 20-, 40-, or 60-micron beads or no implant control. A) Fluorescent microscopy images of IHC for GFAP (green) and fibronectin (red) at 2 wpi. B) Quantification of GFAP$^+$ area per given area of tissue. C) Quantification of fibronectin$^+$ area per given area of tissue. Statistical analysis: Brown-Forsythe and Welch ANOVA with Dunnett's multiple comparisons test. *$p < 0.05$, **$p < 0.01$, ***$p < 0.001$, and ****$p < 0.0001$. Error bars: mean ± standard error of the mean; $n = 4$–5 animals per condition.

apposition (Figure S1C, Supporting Information). Control animals received no implant to the injury but received gelfoam on top of the injured spinal cord to prevent muscular adhesions and control bleeding.[35,36] Glial and fibrotic scarring were characterized 2 weeks post-injury (wpi) by quantification of glial fibrillary acidic protein (GFAP)$^+$ and fibronectin$^+$ tissue areas using longitudinal (Figure S2B, Supporting Information) immunohistochemistry (IHC) (**Figure 2**A). Glial scar tissue forms a physical and chemical barrier that prevents axonal regeneration, and the reduction of glial scarring is linked to successful therapies.[37,38] Tubes composed of 40- and 60-micron beads significantly reduced GFAP$^+$ area (81 500 and 75 500 µm^2/mm^2 tissue) compared to control (123 000 µm^2/mm^2 tissue) (Figure 2B). No significant differences were found between tube treatment groups. Staining for chondroitin sulfate proteoglycan (CSPG) was also conducted to further assess the glial scar environment. CSPG was observed to localize similarly to GFAP on the exterior border of the injury. CSPG was also observed to be abundant in the no-implant control lesion, but largely absent from the injury in all tube conditions (Figure S4A–D, Supporting Information). In murine hemisection models, the fibrotic scar, a dense network of extracellular matrix secreted by infiltrating fibroblasts, forms at the injury epicenter. This matrix represents an additional physical barrier to axon entry.[6,39,40] Tubes composed of all bead sizes reduced area of fibrotic scarring (397 100, 358 800, and 391 500 µm^2/mm^2 tissue for 20-, 40-, and 60-micron tubes, respectively) compared to control (497 900 µm^2/mm^2 tissue) (Figure 2C). No significant differences were found between tube treatment groups. Channels across the fibrotic scar where tubes are present are clearly visible by fibronectin staining, indicating that tubes successfully create paths across the injury.

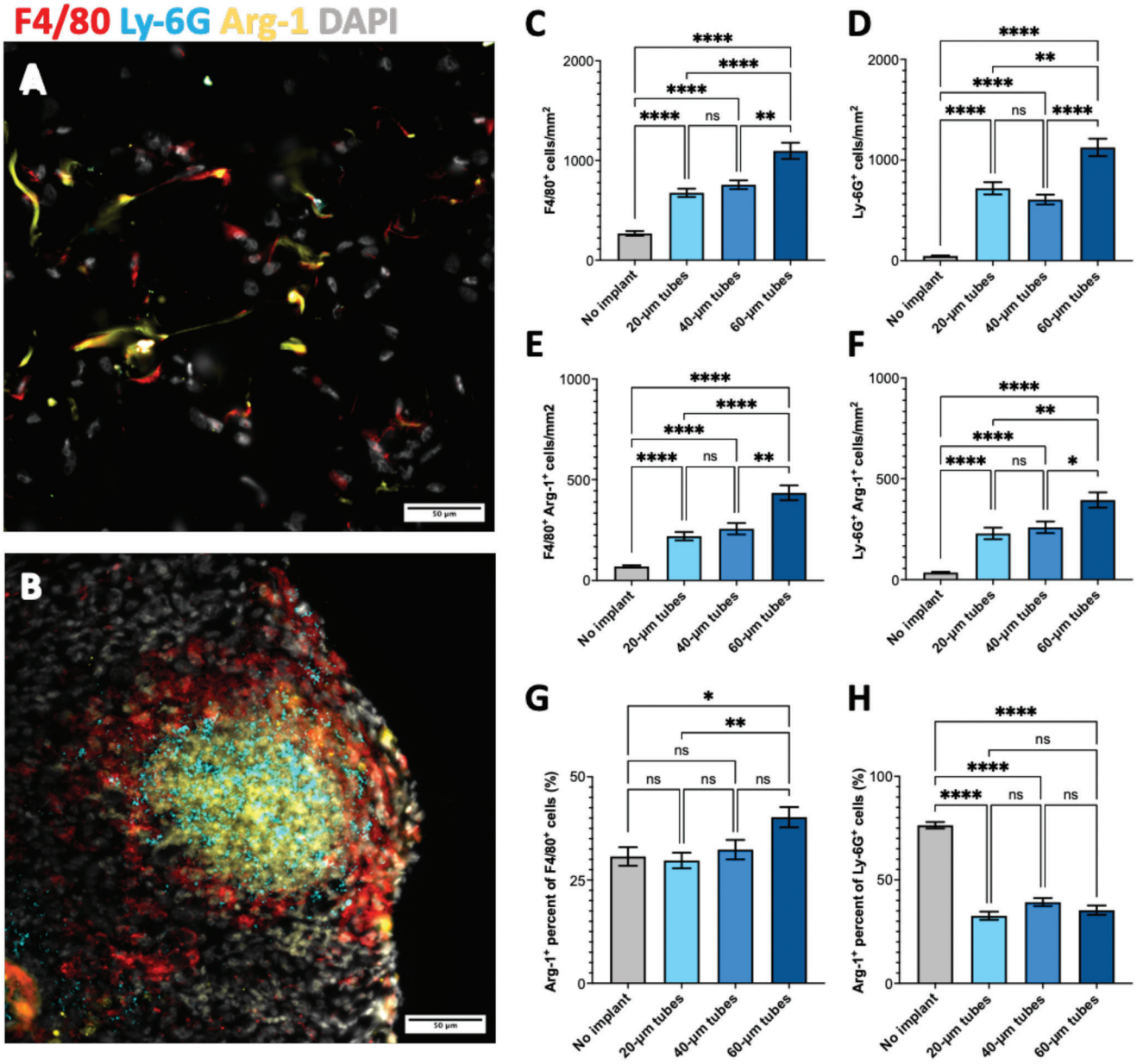

Figure 3. Bead size alters immune cell densities and modulates macrophage phenotype at 1 wpi. Animals were given T9-10 hemisection injuries and subsequently received tubes composed of 20-, 40-, or 60-micron beads or no implant control. Fluorescent microscopy images of IHC for F4/80 (macrophages/microglia, red), Ly-6G (neutrophils, cyan), Arg-1 (alternative activation, yellow), and DAPI (nuclei, gray) in A) no implant and B) 60-micron PEG tubes at 1 wpi. C) Quantification of F4/80$^+$ DAPI$^+$ macrophages/microglia. D) Quantification of Ly-6G$^+$ DAPI$^+$ neutrophils. E) Quantification of F4/80$^+$ DAPI$^+$ Arg-1$^+$ M2 macrophages/microglia. F) Quantification of Ly-6G$^+$ DAPI$^+$ Arg-1$^+$ N2 neutrophils. G) Percent M2 macrophages of total F4/80$^+$ DAPI$^+$ cells. H) Percent N2 neutrophils of total Ly-6G$^+$ DAPI$^+$ cells. Statistical analysis: Brown-Forsythe and Welch ANOVA with Dunnett's multiple comparisons test. *$p < 0.05$, **$p < 0.01$, ***$p < 0.001$, and ****$p < 0.0001$. Error bars: mean ± standard error of the mean; $n = 5$ animals per condition.

2.3. PEG Tubes Increase Immune Cell Density and Influence Immune Phenotype in a Bead Size-Dependent Manner

We next investigated the effect of bead size on innate immune populations present at the injury at an early timepoint. Immune cells in the injury microenvironment were assessed 1 wpi by transverse (Figure S2A, Supporting Information) IHC (**Figure 3**A, B and Figure S5A, Supporting Information). Macrophages and microglia were identified by colocalization of F4/80 and DAPI, and cells with M2 phenotypes were identified by expression of Arginase-1 (Arg-1). Cell density of macrophages/microglia increased in a size-dependent manner (676, 757, and 1097 F4/80$^+$ cells/mm^2 in 20-, 40-, and 60-um tubes, respectively), and all formulations had increased counts compared to control (269 F4/80$^+$ cells/mm^2) (Figure 3C). Similar size-dependent trends were observed for M2 populations

(Figure 3E). Interestingly, the percentage of M2 macrophages was also size-dependent, with tubes composed of 60-micron beads demonstrating a significantly higher proportion of F4/80$^+$ Arg-1$^+$ cells (40.2%) compared to control (30.7%) (Figure 3G).

Neutrophils were identified by colocalization of lymphocyte antigen 6 complex locus G6D (Ly-6G) and DAPI, and cells with N2 phenotypes were identified by expression of Arg-1. The density of neutrophils was increased in all tubes conditions (720, 608, 1126 Ly-6G$^+$ cells/mm^2 in 20-, 40-, and 60-um tubes, respectively) compared to control (47 Ly-6G$^+$ cells/mm^2) (Figure 3D). Similar to macrophages, Arg-1$^+$ cell densities increased with increasing bead size (Figure 3F). Bead size did not affect the proportion of N2 neutrophils, and all tube conditions had significantly lower percentages of Arg-1$^+$ neutrophils compared to control, likely due to the near-negligible Ly-6G$^+$ counts found in the control condition (Figure 3H). No dependence was found on location within the injury for acute immune cell densities (Figure S5B–G, Supporting Information). As tubes composed of 60-micron beads resulted in the lowest GFAP$^+$ tissue area, the highest densities of both macrophages and neutrophils, and the highest proportion of Arg-1$^+$ macrophages, all subsequent studies were performed using this composition.

2.4. PEG Tubes Increase Cell Density of the Chronic Macrophage Surge

In SCI, a distinctive second surge of macrophages is observed at 8 wpi, which we next examined to assess the chronic immune response to tube implantation.[41,42] Immune cells present in the injury microenvironment were assessed 8 wpi by IHC (**Figure 4**A, B and Figure S6A, Supporting Information). The characteristic multiphasic response of macrophages was present in both experimental and control animals, with the second surge being significantly larger than the first in both conditions (Figure 4C). M2 population density demonstrated a similar increase, with animals receiving tubes (1010 F4/80$^+$ Arg-1$^+$ cells/mm^2) having significantly higher cell densities than those receiving control (703 F4/80$^+$ Arg-1$^+$ cells/mm^2) (Figure 4D). While animals receiving tubes had greater M2 cell densities, particularly within the rostral region of the injury (Figure S6B–D, Supporting Information), the proportion of M2 macrophages was found to be comparable between conditions (no implant: 44% vs tubes: 37%) (Figure 4E). Both animals receiving tubes and no implant controls had similar M2 proportions at 8 wpi compared to animals receiving tubes composed of 60-micron beads at 1 wpi (40%).

Unlike macrophages, which exhibit a multiphasic response, neutrophils infiltrate at high rates in the acute injury and quickly decline, maintaining a low, consistent count into the chronic phase.[41] Despite the robust neutrophilic response observed in animals receiving tubes at 1 wpi (1126 Ly-6G$^+$ cells/mm^2), all animals had low neutrophil densities at 8 wpi with no significant difference between animals receiving tubes (144 Ly-6G$^+$ cells mm^{-2}) and those receiving controls (101 Ly-6G$^+$ cells/mm^2) (Figure 4F). Neutrophils in animals receiving tubes were present at greater densities within the rostral portion of the injury (Figure S6E–G, Supporting Information). Counts of N2 neutrophils dropped, with both experimental and control groups showing similar N2 densities (Figure 4G). At 8 wpi, 96% of neutrophils in both conditions were found to have N2 phenotypes (Figure 4H).

2.5. PEG Tubes Improve Locomotor Function

We next examined functional recovery following implantation of tubes composed of 60-micron beads. Open-field locomotion testing was performed using the BMS to assess hindlimb motor function.[24] Significant functional improvement of animals receiving PEG tubes compared to control was observed starting 4 wpi and continued until termination of the study at 8 wpi (**Figure 5**A). At the conclusion of the study, animals receiving tubes averaged scores of 4.3, indicating occasional to frequent plantar stepping. In contrast, control animals averaged 2.6, between extensive ankle movement and occasional to frequent dorsal stepping. To further study hindlimb coordination, ladder beam assessment was performed at 8 wpi.[25] Correct placements of the left hindlimb were counted. Animals receiving PEG tubes had significantly more correct placements than animals receiving no implant control (6.38 vs 3.25) (Figure 5B).

2.6. PEG Tubes Enhance Axonal Regeneration and Remyelination

Given the functional improvement of animals receiving PEG tubes, we next investigated the regeneration of neural populations. Axonal regeneration and remyelination were assessed at 8 wpi by IHC for neurofilament 200 (NF200)$^+$ axons, myelin basic protein (MBP)$^+$ myelin, and myelin protein zero (P0)$^+$ Schwann cell-derived myelin (**Figure 6**A, B and Figure S8A, Supporting Information) as well as by hematoxylin and eosin (H&E) stain (Figure S7A,B, Supporting Information). The number of axons was assessed at rostral, middle, and caudal regions of the injury site, as previously reported.[17,37,43] Animals receiving tubes had significantly greater axon numbers at each location (3.6x, 3.0x, and 2.3x at rostral, middle, and caudal, respectively) compared to animals receiving no implant control (Figure 6C). Axons were identified in both the lumens of tubes and in the inter-tube spaces. Remyelination of regenerated axons was assessed by colocalization of MBP with NF200$^+$ axons. Animals receiving tubes had a greater proportion of myelinated axons (13.7%) than animals receiving no implant control (7.1%) (Figure 6D). Peripheral nervous system Schwann cells were identified by colocalization of MBP and P0 to determine the proportion of axons myelinated by native central nervous system oligodendrocytes. No differences in myelination by either oligodendrocytes or Schwann cells were observed by location within the injury (Figure S8B,C, Supporting Information). No differences in myelination by oligodendrocytes were found between animals receiving tubes and those receiving no implant control (Figure 6E).

3. Discussion

In this report, we demonstrate that MAP tubes exhibit building-block size-dependent modulation of innate immune populations and scarring and, employing the formulation that most attenuates scarring and inflammation, result in enhanced locomotor

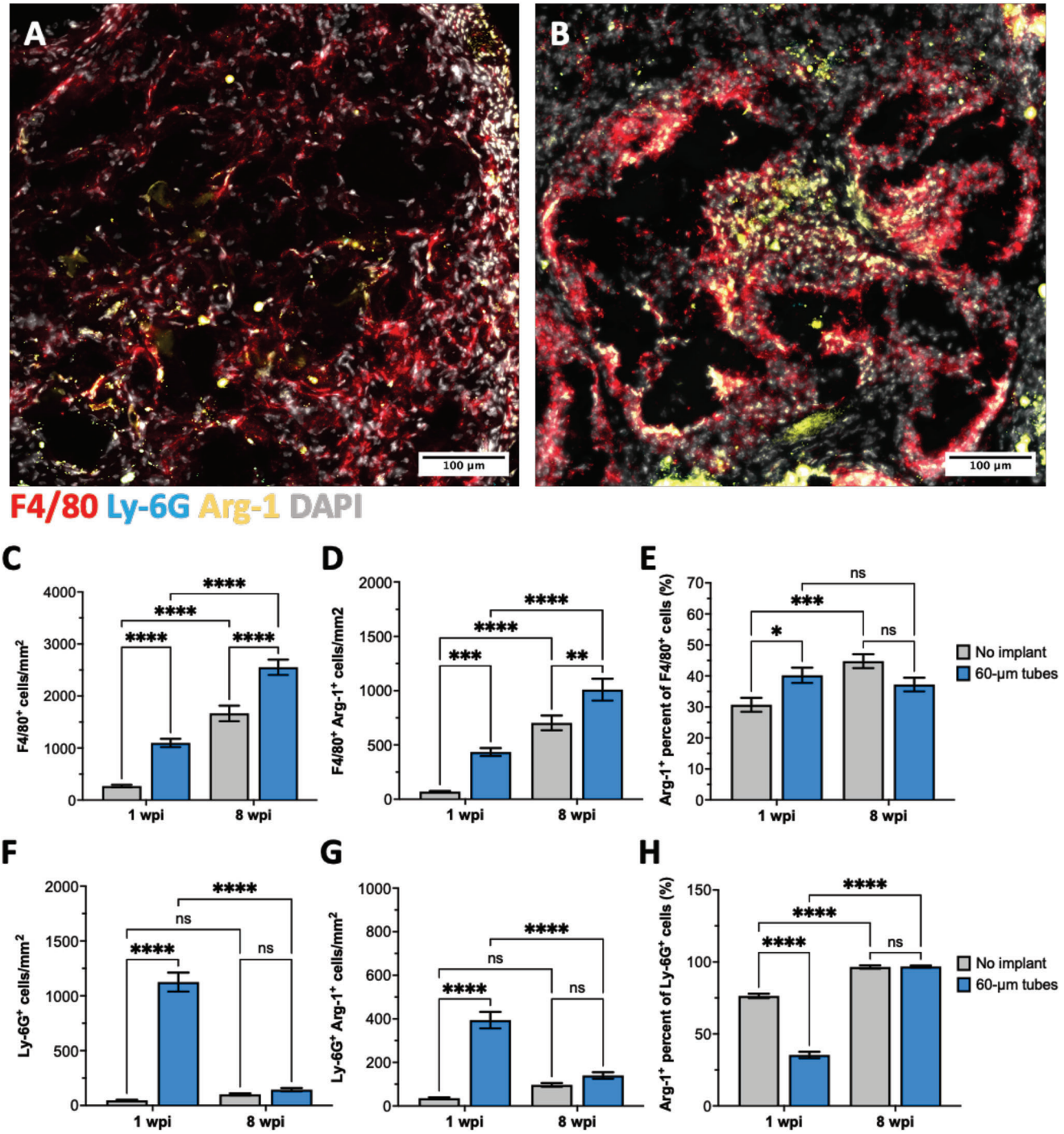

Figure 4. PEG tubes enhance chronic macrophage surge and do not affect chronic neutrophil density. Animals were subjected to T9-10 hemisection injuries and subsequently received tubes composed of 60-micron beads or no implant control. Fluorescent microscopy images of IHC for F4/80 (macrophages/microglia, red), Ly-6G (neutrophils, cyan), Arg-1 (alternative activation, yellow), and DAPI (nuclei, gray) in A) no implant and B) 60-micron PEG tubes at 8 wpi. 1 wpi data from Figure 3 is presented for comparison. C) Quantification of F4/80$^+$ DAPI$^+$ macrophages/microglia. D) Quantification of F4/80$^+$ DAPI$^+$ Arg-1$^+$ M2 macrophages/microglia. E) Percent M2 macrophages of total F4/80$^+$ DAPI$^+$ cells. F) Quantification of Ly-6G$^+$ DAPI$^+$ neutrophils. G) Quantification of Ly-6G$^+$ DAPI$^+$ Arg-1$^+$ N2 neutrophils. H) Percent N2 neutrophils of total Ly-6G$^+$ DAPI$^+$ cells. Statistical analysis: two-way ANOVA with Tukey's multiple comparisons test. *$p < 0.05$, **$p < 0.01$, ***$p < 0.001$, and ****$p < 0.0001$. Error bars: mean ± standard error of the mean; $n = 4$–5 animals per condition.

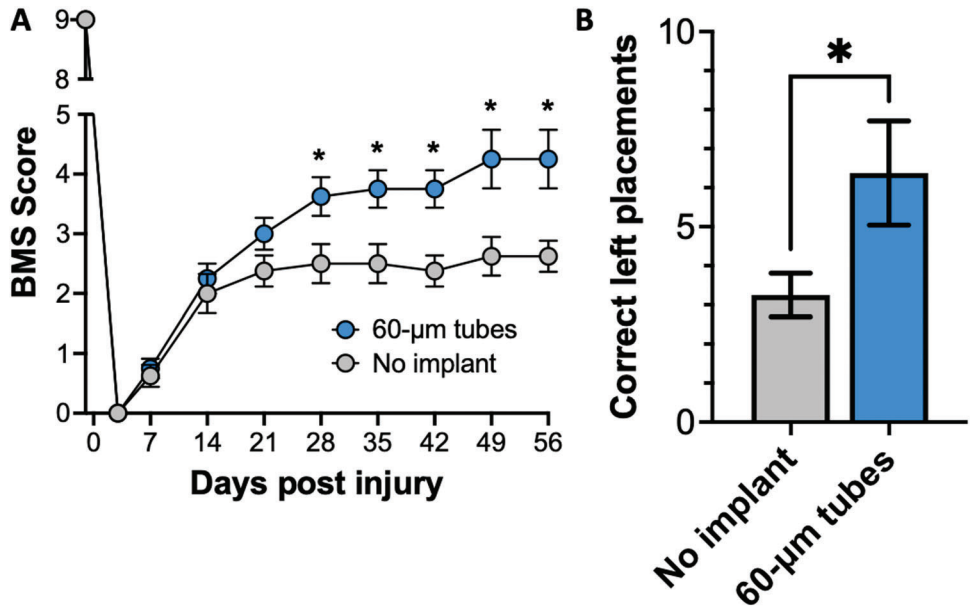

Figure 5. PEG tubes enhance locomotor recovery. Animals were subjected to T9-10 hemisection injuries and subsequently received tubes composed of 60-micron beads or no implant control. Left hindlimb function was assessed weekly for 8 weeks A) by the BMS and at the termination of the study B) by ladder beam walking task. Statistical analysis: BMS was analyzed by two-sample *t*-test at each timepoint. Ladder beam analyzed by two-sample *t*-test with Welch's correction. $*p < 0.05$, $**p < 0.01$, $***p < 0.001$, and $****p < 0.0001$. Error bars: mean ± standard error of the mean; $n = 8$ animals per condition.

recovery and neuronal regeneration following SCI. Biomaterial bridges have been central strategies in the treatment of models of penetrating injury, which generally do not exhibit substantial recovery of function.[44] Our prior work investigated the use of PEG tubes composed of polydisperse beads that can be employed as modular, adaptable bridges to provide uniaxial guidance for regeneration.[17] This work presents several variations to these tubes: the introduction of a microengineered emulsion-to-powder technique to preserve hydrogel architecture, the inclusion of 4-arm PEG in the secondary crosslinking solution to promote polymer branching, and the use of low-polydispersity beads. Low-polydispersity MAPs offer several properties which enhance their utility relative to high-polydispersity MAPs as therapeutics for SCI.[19–21,18] This study investigated these MAP tubes for their ability to modulate scarring and inflammation and to support regeneration and improve functional recovery.

Both fibrotic and glial scarring were reduced at 2 wpi in animals that received PEG tubes. In SCI, the fibrotic scar represents a physical barrier to entry of regenerating axons.[6,39,40] While the fibrotic scars of hemisection models fill the injury, those of contusion models tend to form thin, dense depositions at the interface of the necrotic cavity and the glial scar.[39,45] Tubes composed of all bead sizes reduced fibronectin$^+$ area by 20%–28% and formed visually identifiable conduits across the injury with no significant dependence on bead size. MAPs have been shown to ameliorate fibrosis following myocardial infarction and facilitate regeneration of functional tissues.[46] As such, reduction of fibrotic scarring in SCI may allow for the formation of a regenerated proneural matrix, as indicated by the subsequent axon ingrowth and enhanced locomotor recovery described in this study. The glial scar, produced by activated astrocytes, similarly forms a physical and chemical barrier that limits axonal re-entry to the injury. As such, reduction of the glial scar is necessary for promoting regeneration following SCI. Conversely, the presence of some degree of gliosis is critical for confinement of the injury, with ablation of reactive astrocytes, and therefore elimination of the glial scar, resulting in impaired functional outcomes.[47] Given this dual-role, reduction, but not elimination, of the glial scar is widely hypothesized to yield the best outcomes for biomaterial therapies following SCI.[38] As opposed to the bead size agnostic reduction of the fibrotic scar, glial scarring was attenuated in a size-dependent manner with only tubes of 40- and 60- micron beads significantly reducing GFAP$^+$ area compared to control. Tubes composed of 60-micron beads attenuated the glial scar by 39%, demonstrating successful reduction, but not elimination, of the scar. The MAP-mediated reduction of astrocytic scarring has also been investigated in models of stroke.[30,18,48] This cross-pathology reduction of glial scarring indicates that MAPs may serve more widely as an approach to reduce gliosis following trauma to the CNS.[4,49] Collectively, these findings demonstrate that PEG tube implantation attenuates both fibrotic and glial scarring in SCI and creates a more permissive environment for neural regeneration.

PEG tube implantation modulated the innate immune response at both acute and chronic time points. In untreated SCI, the early immune response is typically characterized by an influx of neutrophils, peaking at day 1 and resolving by day 3, after which neutrophils maintain a small and constant presence into the chronic stages of injury.[1,41] At 1 wpi, PEG tubes increased neutrophil density in a bead size-dependent manner, with tubes composed of 60-micron beads resulting in a 24-fold increase in the density of neutrophils present compared to control. While a small increase in neutrophil count was identified in previous studies using tubes composed of high-polydispersity beads,[17] the robust increase in neutrophil density observed in tubes

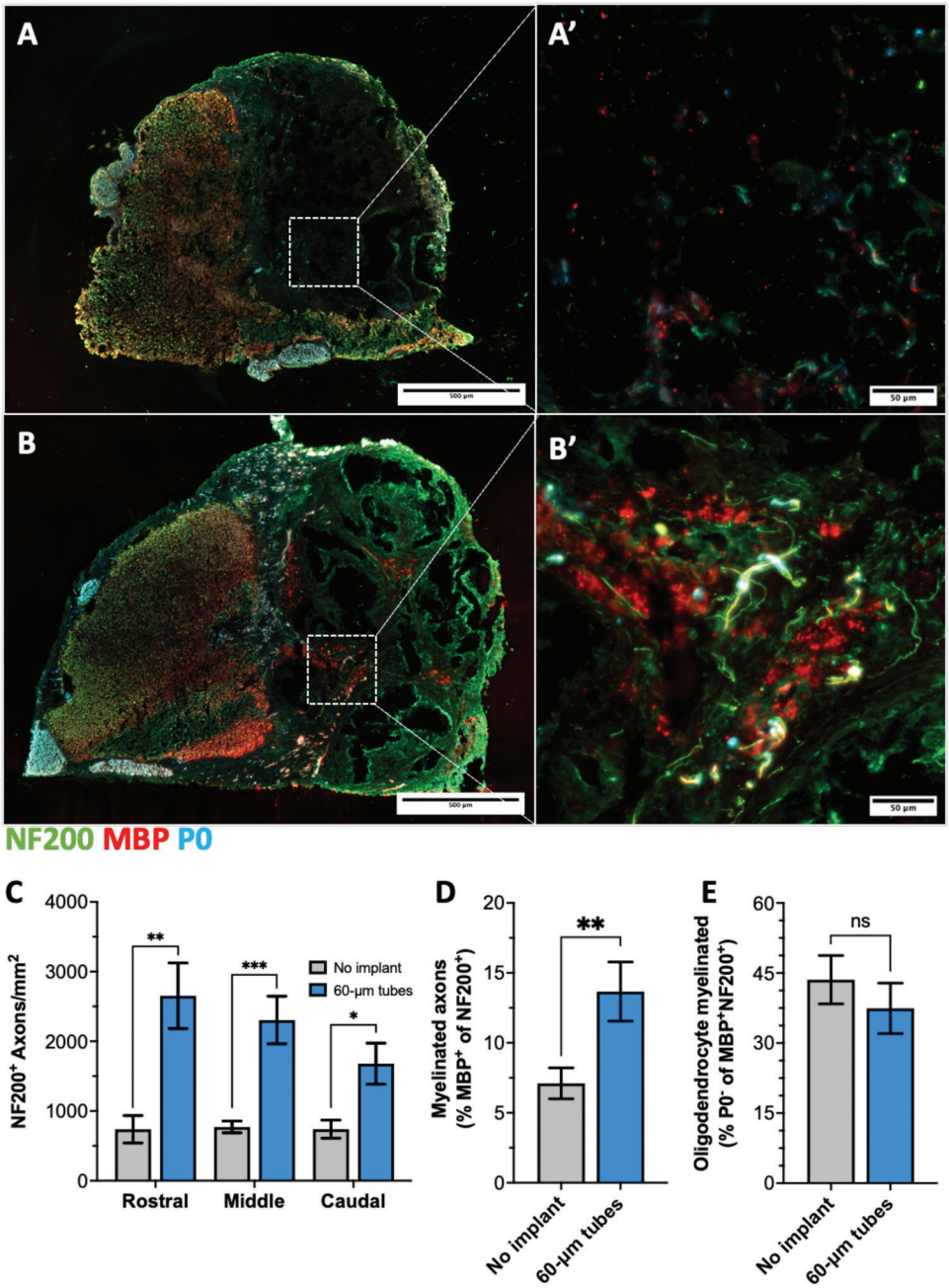

Figure 6. PEG tubes promote axonal regeneration and remyelination. Animals were subjected to T9-10 hemisection injuries and subsequently received tubes composed of 60-micron beads or no implant control. Fluorescent microscopy images of IHC for NF200 (axons, green), MBP (myelin, red), and P0 (Schwann cells, cyan) in A) no implant and B) 60-micron PEG tubes at 8 wpi. A') no implant at high magnification. B') 60-micron PEG tubes at high magnification. C) Quantification of axons per square millimeter at rostral, middle, and caudal locations of the injury. D) Percent of $NF200^+$ axons colocalized with MBP^+ myelin of total $NF200^+$ axons. E) Percent of $NF200^+$ MBP^+ $P0^-$ oligodendrocytes of total $NF200^+$ MBP^+ myelinated axons. Axons were analyzed by multiple *t*-test with Holm-Šídák multiple comparisons and myelination was analyzed by two-sample *t*-test with Welch's correction. $^*p < 0.05$, $^{**}p < 0.01$, $^{***}p < 0.001$, and $^{****}p < 0.0001$. Error bars: mean ± standard error of the mean; $n = 4$ animals per condition.

composed of low-polydispersity beads is a novel finding. These differences may be influenced, in small part, by the method of analysis (flow cytometry vs immunohistochemistry) but are more likely the effect of the different compositions of tubes employed.[50] While the neutrophilic response had resolved appropriately by 8 wpi, the presence of a large neutrophil population at 1 wpi is highly unusual. Though neutrophils are canonically classified as deleterious in SCI, emerging evidence suggests that immature and alternatively activated N2 neutrophils may have neuroprotective properties.[51,52] With 32%–39% of the identified neutrophils expressing Arg-1 in tube-implanted mice at 1 wpi, further studies are necessary to thoroughly investigate

their phenotypes and to explain this prolonged infiltration. In the timeline of SCI, the early neutrophil surge is followed by a peak of macrophages on day 7, which resolves almost entirely by day 14. The macrophage response is multiphasic, with a larger, chronic peak occurring 60 days post-injury.[41,42] PEG tubes increase macrophage density in a bead size-dependent manner at 1 wpi, with tubes composed of 60-micron beads resulting in a 4-fold increase of macrophages compared to control. Qualitatively, a patterning of immune cells can be observed at 1 wpi, with macrophages associating primarily with the polymer walls and neutrophils present throughout both the walls and lumens. The neutrophilic response can likely be attributed to a foreign body response to the implant. The enrichment of macrophages in the tube wall must be the result of either monocyte migration specifically to the porous wall or an extended half-life mediated by porosity-directed differentiation.[53] At 8 wpi, the second surge of the multiphasic macrophage response was increased by 1.5-fold by implantation of tubes composed of 60-micron beads compared to control. Tubes of 60-micron beads increased the proportion of Arg-1$^+$ macrophages by 31% compared to control at the early timepoint, while there was no significant difference in M2/M1 proportion found between tubes and control at the late timepoint. The early polarization of macrophages toward an M2 phenotype can likely be attributed to spatial confinement mediated by material pores[20] and, while the phenotypic effect of the tubes appears to be lost over time, early polarization toward alternative activation limits neurotoxicity and promotes enhanced regeneration.[54,55] M1 macrophage presence in the early injury is critical for clearance of myelin and cell debris, but this inflammatory phenotype is often over-represented in SCI, leading to a non-resolving chronic inflammatory state.[42] By enhancing the proportion of macrophages with M2 characteristics early in the injury timeline, the immune trajectory can be corrected to facilitate a healthy wound healing cascade, ultimately leading to improved regeneration and enhanced recovery of function.[54] While Arg-1 expression is associated with alternatively activated phenotypes, this marker is not comprehensive and further studies will be required to robustly identify the immune phenotypes present in the injury microenvironment. Together, these findings indicate that PEG tubes have unique immunomodulatory effects on the injury microenvironment and can contribute to the attenuation of secondary injury by inflammation following SCI.

Implantation of 60-micron PEG tubes resulted in robust regeneration of neural tissue, ultimately resulting in enhanced recovery of locomotor function. Axons in the CNS possess the inherent potential for regeneration but are limited by a number of factors, including the glial and fibrotic scars, the inflammatory environment resulting from secondary injury, and intraneuronal mechanisms preventing elongation.[56] Through mechanisms such as endogenous regeneration, sprouting, and structural plasticity, a number of axons enter the untreated injury but primarily fail to form functional circuitry. The goal of biomaterial therapies in SCI is to facilitate entry of greater numbers of neuronal populations to increase the likelihood of formation of functional synapses.[57–59] On average, animals receiving tubes had 3.2-fold greater axon counts throughout the injury compared to animals receiving no implant controls. Compared to previous reports of PLG bridges with similarly sized channels, animals receiving PEG tubes had nearly two times as many axons per square millimeter.[43] This increase can be attributed to the intra-tube voids, where axons were observed at high densities, which increase the available cross-sectional area by 43% compared to a non-modular equivalent.[23] Further, axons were also observed within the polymer walls of tubes, indicating that some extent of material degradation and absorption had occurred due to the plasmin-degradable peptide crosslinker. This axonal ingrowth supports the significant locomotor recovery in animals receiving tubes, both by the BMS and the ladder beam assessment. The axon counts reported in this study suggest that greater functional improvements may be possible using combinatorial therapies. Only 13.7% of axons in animals receiving tubes were myelinated – a substantially lower proportion than observed previously in the uninjured spinal cord or regenerating through PLG bridges.[8,12,43] The modular and hydrophilic properties of PEG tubes make them an excellent platform for integration of other strategies to augment myelination. Combining PEG tubes with other treatments known to enhance myelination of regenerating axons, such as delivery of neurotrophin-3, brain-derived neurotrophic factor, interleukin-10, or oligodendrocyte progenitor cells, may further improve functional recovery.[11,16,43,60–62] Alternatively, electrical stimulation may promote axonal elongation and neuroplasticity that may support axonal guidance and induce the formation of de novo synapses.[63] In this study, MAP tubes were implanted immediately following injury, a model which likely cannot be employed in clinical translation. In models of stroke, MAP gels successfully mediate remodeling of the CNS when injected 5 days postinjury and previous studies in SCI have demonstrated the feasibility of biomaterial intervention in the chronic injury phase.[12,30] Together, these studies suggest that post-injury implantation may be feasible as a route for clinical translation, although further studies will be required to thoroughly assess the effects of intervention at nonacute timepoints. Collectively, these findings demonstrate that PEG tubes support the regeneration of axons and facilitate recovery of function below the level of injury following SCI.

4. Conclusion

In this work, we investigated the effects of building-block size on MAP gels with tubular geometries as bridges for the treatment of SCI. Tubes composed of high-fidelity, low-polydispersity 20-, 40-, and 60-micron beads were found to have size-independent void fractions and swelling ratios upon rehydration, and size-dependent pore cross-sectional areas and compressive moduli. Further, these constructs can be produced as off-the-shelf products and customized in terms of number and length to adapt to unique injury geometries. MAP tubes modulated macrophage and neutrophil density and phenotype in a bead size-dependent manner while all formulations attenuated scarring in a largely size-independent manner. Using tubes composed of 60-micron beads, we observed enhanced locomotor recovery via the BMS and ladder beam assessment. This recovery can be attributed to the substantial ingrowth of axons and remyelination through both tube lumens and the inter-tube space. Additional studies that utilize this system as a biomaterial platform for immunomodulatory, neuroprotective, and regenerative approaches will further empower MAP tubes as potential tools for the treatment of clinical SCI. Collectively, these studies demonstrate that

bead size in MAP gel construction impacts the host immune response and subsequent neuronal regeneration, highlighting the potential of PEG tubes as a biomaterial platform for the treatment of SCI.

5. Experimental Section

Microfluidic Droplet Generator Design and Fabrication: Beads were generated using a custom-designed microfluidic droplet-generating device. Devices were designed in AutoCAD, and master molds were fabricated using a SU-8 negative photoresist (Kayaku, Westborough, MA). PDMS (1:10 crosslinker:base ratio) devices were replica cast from SU-8 masters. Holes were punched through the PDMS at the entry and exit ports of each device using biopsy punches. Devices were then cleaned, plasma etched for 1 min, and bonded to glass slides.

Production of PEG Microgels: For microgel fabrication, 80 mg of 8-arm PEG-maleimide (20 kDa, JenKem, Plano, TX) was suspended in 400 µL HEPES (0.1M, $pH = 1.0$, Fisher Scientific, Waltham, MA). Plasmin-sensitive YKND cross-linking peptide[26] (Ac-GCYKNDGCYKNDCG; Genscript, Piscataway, NJ) was suspended first in 40 µL dimethylsulfoxide (Sigma Aldrich, Saint Louis, MO) and subsequently diluted with 360 µL HEPES (0.1M, $pH = 1.0$). The PEG solution was then mixed with the YKND solution, constituting the aqueous phase for droplet generation. NOVEC 7500 engineered fluid (3 M, Saint Paul, MN) was mixed at a 4:1 ratio with 008-Fluorosurfactant (5 w/v%, Ran Biotechnologies, Beverly, MA), constituting the organic phase. The organic phase was passed through a 0.22 µm filter (Fisher Scientific, Waltham, MA) to remove any debris that could interfere with flow regimes. Organic flow rate for all microfluidic devices was 1 ml h^{-1}. Aqueous flow rates for 20-, 40-, and 60-micron microfluidic devices were 0.2-, 0.35-, and 0.5-mL h^{-1}, respectively. 12 µL triethylamine (Millipore Sigma, Darmstadt, Germany) was added to 488 uL of fresh NOVEC 7500 and this solution was added, dropwise, to the collected emulsion under gentle agitation. The emulsion was then incubated at 37 °C for 1 h to allow for the completion of crosslinking. The microengineered emulsion-to-powder technique[28] was employed – the emulsion was flash-frozen in liquid nitrogen and lyophilized for at least 24 hours at −105 °C and 0.01 mbar (Freezone 4.5L, Labconco, Kansas City, MO). Lyophilized materials were stored at room temperature in a desiccator under vacuum.

Production of PEG Tubes: For fabrication of PEG tubes, 20 mg of lyophilized particles were added to a microcentrifuge tube and rehydrated with 120 µL of 1 w/v% 2-hydroxy-4′-(2-hydroxy-ethoxy)−2-methylpropiophenone (Irgacure 2959, Sigma Aldrich, Saint Louis, MO), 1 w/v% 4-arm PEG-maleimide (10 kDa, JenKem, Plano, TX), and 20 v/v% N-vinylpyrrolidinone (Sigma Aldrich, Saint Louis, MO) in HEPES (0.1M, $pH = 7.4$). Hydrated particles were packed into 400 µm inner diameter borosilicate precision capillary tubes (Fisher Scientific, Waltham, MA). Lumens were formed by inserting 250 µm pins (Austerlitz 000 insect pins, Fine Science Tools, Foster City, CA) with custom alignment pins (360 µm outer diameter, 250 µm inner diameter, New England Small Tubes, Litchfield, NH). Constructs were then exposed to an ultraviolet lamp (Omnicure series 1500, Excelitas, Waltham, MA) for 6 minutes at 100% power to facilitate full completion of the crosslinking reaction. Following photoinitiated crosslinking, PEG tubes were pushed through capillaries using the 250 µm pins and custom alignment pins as supports to maintain structure. The alignment pin was then used as a plunger to remove the tube from the fine insect pin directly into 1.5 mL of deionized water. Tubes were washed in deionized water without agitation, so as not to disrupt the tubular geometry, for at least 20 min to remove any unreacted crosslinking solution. Tubes were removed from the deionized water wash, flash frozen at −80 °C and lyophilized for at least 12 hours. Tubes were then cut to 1.7 mm. Lyophilized materials were stored at room temperature in a desiccator under vacuum.

Characterization of Microgels and Tubes: Microgels in the emulsion were imaged with an Axio Observer Z1 (Zeiss, Oberkochen, Germany) at 10x using an ORCA-Flash 4.0 V2 Digital CMOS camera (Hamamatsu Photonics, Hamamatsu City, Shizuoka, Japan). Microgel size distributions were characterized using CellProfiler[64] (www.cellprofiler.org). Tubes were imaged at 10x prior to lyophilization, in their lyophilized state, and following rehydration to assess the effects of lyophilization on tube architecture. For assessment of porosity, Cy5-maleimide (1 mM, Lumiprobe, Cockeysville, MA) was included in the aqueous phase of droplet generation. Microgels were crosslinked in bulk 150 µm sheets using the same chemistry described in the production of PEG tubes. For comparison of materials pre- and post-lyophilization, sheets were either prepared freshly on the day of imaging or pre-prepared, lyophilized, and rehydrated in 2 mL of deionized water for 30 min on the day of imaging. Sheets were then submerged in a solution of fluorescein isothiocyanate-dextran (FITC-dextran, 100 mM, Millipore Sigma, Saint Louis, MO) and imaged with a stack distance of 1.16 µm. Images were processed in FluoRender. Average pore size and void fraction were determined by the presence of FITC-dextran using FIJI.[65] For measurements of swelling upon rehydration, 1.7 mm lengths of tubes were cut while lyophilized and rehydrated in 100 µL of deionized water. Tubes were rehydrated for 30 min and subsequently measured with calipers. Compressive moduli were measured using a microsquisher (Cell Scale, Ontario, CA). Slabs of crosslinked beads were used to eliminate the confounds associated with the complex tubular geometry. Materials were lyophilized and rehydrated prior to testing, such that they accurately reflect the materials employed in vivo. For comparison of materials pre- and post-lyophilization, slabs were either prepared freshly on the day of testing or pre-prepared, lyophilized, and rehydrated in 2 mL of deionized water for 30 minutes on the day of testing. A 59.5 mm cantilever beam with a 4 mm parallel compression plate were used.

Surgical Implantation of PEG Tubes: All animal work was performed with prior approval and in accordance with the Institutional Animal Care and Use Committee (IACUC) guidelines at the University of Michigan (approval number IACUC PRO00009683). A T9-10 lateral hemisection injury was performed on 6–8 week-old female C57BL/6J mice (Jackson Laboratory, Bar Harbor, ME) as previously described.[17,43,23] Mice were anesthetized with 2% isoflurane and given a local anesthetic (1 mg kg^{-1} bupivacaine, Medline Industries, Northfield, IL) prior to surgery. A 2 cm incision was made in the skin and dorsal laminectomy was performed on both the T9 and T10 vertebrae. A 2.25 mm lateral hemisection was then removed. 5 individual PEG tubes were inserted into the injury site and allowed to hydrate into apposition with the rostral and caudal surfaces of the spinal cord. Gelfoam (Ethicon, Raritan, NJ) was used to secure the injury site and prevent muscular adhesion to the spinal cord. Control animals received no implant to the injury site but received gelfoam on top of the injured spinal cord to prevent muscular adhesions and control bleeding. Muscle was then sutured, and skin was stapled. Mice received post-operative antibiotics (2.5 mg kg^{-1} enrofloxacin, Bayer, Leverkusen, Germany) once a day for 14 days, long-acting analgesics following surgery, and 2 days post-injury (Ethiqa, MWI Veterinary Supply, Boise, ID), and support hydration once a day for 5 days (1 mL lactated ringer's solution, MWI Veterinary Supply, Boise, ID). Staples were removed 10 days post-injury and bladders were expressed twice daily until bladder function was recovered. Surgical controls were used to limit injury variation, including the order of incisions and verification of the absence of damage to the contralateral tissue. Exclusion criteria include any deviations to surgical controls, as well as major variance to the recovery timeline, including the ability to perform ipsilateral hindlimb movement at three days post-injury, indicating incomplete hemisection, or the inability to perform contralateral hindlimb movement by day 14, indicating full transection. Mice were euthanized and spinal cord segments T8-11 were collected at 1, 2, or 8 wpi.

Histology and Immunohistochemistry: Isolated spinal cords were immediately flash frozen in 2-methylbutane (Fisher Scientific, Waltham, MA) and embedded in optimal cutting temperature compound (Fisher Scientific, Waltham, MA) with 20 w/w% sucrose (Sigma Aldrich, Saint Louis, MO). Tissues were then cryosection at 14 µm transversely (1 and 8 wpi tissues) or longitudinally (2 wpi). For H&E staining, samples were fixed with 4% paraformaldyhyde (ThermoFisher Scientific, Waltham, MA) and then stained with an H&E staining kit (Abcam, Cambridge, UK) according to the manufacturer's recommendations. For IHC, samples were fixed, permeabilized, blocked as necessary, and incubated overnight at 4 °C with

Table 1. Primary antibodies used for immunohistochemistry.

Primary Antibody	Company	Catalogue number	Concentration
GFAP	Aves Labs	GFAP	1:250
Fibronectin	ThermoFisher Scientific	15 613-1-AP	1:500
CSPG	Millipore Sigma	Ab5320	1:100
F4/80	Bio-Rad	MCA497GA	1:1000
Ly-6G	Biolegend	127 602	1:1000
Arg-1	ThermoFisher Scientific	PA5-29645	1:500
NF200	Millipore Sigma	N4142	1:200
MBP	Bio-Rad	MCA409S	1:200
P0	Aves Labs	PZO	1:250

primary antibodies (**Table 1**). Tissues were then incubated for 2 hours with species-specific secondary antibodies (**Table 2**). For immune cell identification, 6 tissues were selected randomly from the rostral, middle, and caudal locations of the injury for each animal. For visualization of glial and fibrotic scarring, as well as CSPG, 3 tissues were selected from the center of the spinal cord for each animal. For identification of axons and oligodendrocytes, 6 tissues were selected randomly from the rostral, middle, and caudal locations of the injury for each animal. Tissues were imaged on an Axio Observer Z1 using an ORCA-Flash 4.0 V2 Digital CMOS camera. All immunohistochemistry images presented were adjusted for brightness and contrast appropriately to provide accurate representations.

Quantification of Glial and Fibrotic Scarring: For quantification of glial and fibrotic scarring, images were exported as.CZI files and converted to a single channel .H5 files in CellProfiler. Files were ported to Ilastik[66] (www.ilastik.org), where pixel classification was performed. Glial scarring was identified by $GFAP^+$ activated astrocytes. Fibrotic scarring was identified by $fibronectin^+$ extracellular matrix. Results of these quantifications are reported as the marker-positive area divided by the marker-negative area for a given 3000 × 4000 pixel section of the tissue centered around the injury.

Quantification of Immune Cells: For quantification of immune cells and immune cell phenotypes, images were exported as.CZI files and converted to a single channel .H5 files in CellProfiler. Files were ported to Ilastik,[66] where pixel classification was performed. Injury areas were identified using the polygon tool in FIJI and saved as masks. Only immune cells within the masked area were used for the assessment of immune cell densities and phenotypes. The area of each mask was calculated in mm^2, and immune cell counts were normalized to the identified injury area to provide total immune cell densities within the injury microenvironment. Immune cells and their phenotypes were identified by colocalization with DAPI. Only cells present in the injury area were reported. Macrophages and activated microglia were identified as $F4/80^+$ $DAPI^+$. Neutrophils were identified as $Ly\text{-}6G^+$ $DAPI^+$. Anti-inflammatory M2 macrophage/microglia were identified as $Arg\text{-}1^+$ $F4/80^+$ $DAPI^+$ and inflammatory macrophage/microglia were identified as $Arg\text{-}1^-$ $F4/80^+$ $DAPI^+$. Anti-inflammatory N2 neutrophils were identified as $Arg\text{-}1^+$ $Ly\text{-}6G^+$ $DAPI^+$ and inflammatory classically activated N1 neutrophils were identified as $Arg\text{-}1^-$ $Ly\text{-}6G^+$ $DAPI^+$.

Behavioral Tests for Locomotor Function: The Basso Mouse Scale was used to evaluate locomotive recovery in mice. Mice were acclimated to the open field for 5 days prior to testing and a pre-surgical timepoint was taken to ensure that no abnormal gait patterns were present in mice used for studies. Two researchers scored mice on ankle mobility, hindlimb placement and stepping, coordination, and trunk stability. Only the ipsilateral hindlimb was scored due to the unilateral nature of the hemisection model. In the case of researcher disagreement, the lower score was taken. Mice were scored at 3 days post-injury and then weekly from 1 week to 8 weeks postinjury.

Ladder beam assessment was performed at 8 wpi to quantitatively gauge locomotive function. Mice were acclimated to the ladder beam apparatus for 3 days prior to testing. Animals were recorded across a 50-rung region of the ladder and left hindlimb placement was assessed. Placement was deemed correct if 1) a complete placement of the paw was performed, with all toes facing forward and the palm on the rung, 2) a partial placement with weight bearing was performed, with toes curled or an uncentered palm, or 3) the animal skipped a rung where both the preceding and following rungs were correct placements. All other steps, including misses and slips, were not counted as correct.

Quantification of Axons and Myelination: For quantification of regenerated and myelinated axons, images were exported as.CZI files and injury areas were identified in FIJI. A hessian filter was applied in Cellprofiler and discreet objects were identified.[67] Only those objects present in the injury area are reported. Axons were identified as $NF200^+$. Myelinated axons were identified as $NF200^+$ MBP^+. Oligodendrocyte myelinated axons were identified as $NF200^+$ MBP^+ $P0^-$.

Statistics: Statistical analyses were performed in GraphPad Prism 9. All values are expressed as the mean ± standard error of the mean. Equal variance was assessed for each study and appropriate analyses were selected. For in vitro characterization studies, $n = 3$ samples per condition were analyzed by one-way ANOVA with Tukey's multiple comparisons test. For scarring studies, $n = 4$–5 animals per condition were analyzed by Brown-Forsythe and Welch ANOVA with Dunnett's multiple comparisons test. For acute immune infiltration studies, $n = 5$ animals per condition were analyzed by Brown-Forsythe and Welch ANOVA with Dunnett's multiple comparisons test. For chronic immune infiltration studies, $n = 4$–5 animals per condition were analyzed by two-way ANOVA with Tukey's multiple comparisons test. For locomotor function, $n = 8$ animals per condition; BMS was analyzed by two-sample *t*-test at each timepoint and ladder beam was analyzed by two-sample t-test with Welch's correction. For axon regeneration and remyelination, $n = 4$ animals per condition; axons were analyzed by multiple *t*-test with Holm-Šídák multiple comparisons, and myelination was analyzed by two-sample *t*-test with Welch's correction. For comparison of freshly made versus rehydrated materials, $n = 3$ samples per condition; all properties were analyzed by multiple *t*-test with Holm-Šídák multiple comparisons. For all comparisons by location within the injury for acute immune cells, chronic immune cells, and meylination, $n = 4$–5 animals per condition; all analyses by two-way ANOVA with Tukey's multiple comparisons. The *p*-values for statistical significance are represented with stars (Unless otherwise noted: $*p < 0.05$, $**p < 0.005$, $***p < 0.0005$, $****p < 0.0001$).

Table 2. Secondary antibodies used for immunohistochemistry.

Secondary Antibody	Company	Catalog number	Concentration
Mouse anti-rat IgG2b 660	ThermoFisher Scientific	50-4815-82	1:100
Mouse anti-rat IgG2a 570	ThermoFisher Scientific	41-4817-82	1:100
Goat anti-rabbit IgG 488	ThermoFisher Scientific	A-11008	1:1000
Goat anti-chicken IgY 488	ThermoFisher Scientific	A-11039	1:1000
Goat anti-rabbit IgG 568	ThermoFisher Scientific	A-11011	1:1000
Goat anti-rat IgG 555	ThermoFisher Scientific	A21434	1:1000
Donkey anti-chicken IgY 633	Millipore Sigma	SAB4600127	1:1000

Supporting Information

Supporting Information is available from the Wiley Online Library or from the author.

Acknowledgements

The authors would like to thank the National Institutes of Health (R01NS117103-01 and R01AI148076) and all members of the Shea lab at the University of Michigan for their support and mentorship. This work was made possible in part by software funded by the NIH: FluoRender: Visualization-Based and Interactive Analysis for Multichannel Microscopy Data, 1R01EB023947-01, and the National Institute of General Medical Sciences of the National Institutes of Health under grant numbers P41 GM103545 and R24 GM136986.

Conflict of Interest

The authors declare no conflict of interest.

Data Availability Statement

The data that support the findings of this study are available from the corresponding author upon reasonable request.

Keywords

microporous annealed particles, modular biomaterials, spinal cord injury, tissue repair

Received: August 1, 2023
Revised: September 10, 2023
Published online:

[1] A. Alizadeh, S. M. Dyck, S. Karimi-Abdolrezaee, *Front. Neurol.* **2019**, *10*, 282.
[2] D. J. Hellenbrand, C. M. Quinn, Z. J. Piper, C. N. Morehouse, J. A. Fixel, A. S. Hanna, *J. Neuroinflammation* **2021**, *18*,284.
[3] S. Okada, M. Hara, K. Kobayakawa, Y. Matsumoto, Y. Nakashima, *Neurosci Res* **2018**, *126*, 39.
[4] M. T. Fitch, J. Silver, *Exp. Neuro. I.* **2008**, *209*, 294
[5] M. L. Lemons, D. R. Howland, D. K. Anderson, *Exp. Neruol.* **1999**, *160*, 51.
[6] Z. Li, S. Yu, X. Hu, Y. Li, X. You, D. Tian, L. Cheng, M. Zheng, J. Jing, *Front. Cell Neurosci.* **2021**, *15*, 720938.
[7] S. Liu, Y. Y. Xie, B. Wang, *Neural Regen Res* **2019**, *14*, 1352.
[8] H. M. Tuinstra, D. J. Margul, A. G. Goodman, R. M. Boehler, S. J. Holland, M. L. Zelivyanskaya, B. J. Cummings, A. J. Anderson, L. D. Shea, *Tissue Eng. Part A* **2014**, *20*, 1027.
[9] K. Pawar, B. J. Cummings, A. Thomas, L. D. Shea, A. Levine, S. Pfaff, A. J. Anderson, *Biomaterials* **2015**, *65*, 1.
[10] L. De Laporte, A. Lei Yan, L. D. Shea, *Biomaterials* **2009**, *30*, 2361.
[11] H M. Tuinstra, M O. Aviles, S. Shin, S J. Holland, M L. Zelivyanskaya, A G. Fast, S Y. Ko, D J. Margul, A K. Bartels, R M. Boehler, B J. Cummings, A J. Anderson, L D. Shea, *Biomaterials* **2012**, *33*, 1618.
[12] D. R. Smith, C. M. Dumont, A. J. Ciciriello, A. Guo, R. Tatineni, M. K. Munsell, B. J. Cummings, A. J. Anderson, L. D. Shea, *ACS Biomater. Sci. Eng.* **2019**, *5*, 6679.
[13] B. A. Breen, H. Kraskiewicz, R. Ronan, A. Kshiragar, A. Patar, T. Sargeant, A. Pandit, S. S. McMahon, *ACS Biomater. Sci. Eng.* **2017**, *3*, 1287.
[14] L. C. Grous, J. Vernengo, Y. Jin, B. T. Himes, J. S. Shumsky, I. Fischer, A. Lowman, *J Neurosurg Spine* **2013**, *18*, 641.
[15] A. J. Ciciriello, D. R. Smith, M. K. Munsell, S. J. Boyd, L. D. Shea, C. M. Dumont, *ACS Biomater. Sci. Eng.* **2020**, *6*, 5771.
[16] A. J. Ciciriello, D. R. Smith, M. K. Munsell, S. J. Boyd, L. D. Shea, C. M. Dumont, *Biotechnol. Bioeng.* **2021**, *118*, 2609.
[17] C. M. Dumont, M. A. Carlson, M. K. Munsell, A. J. Ciciriello, K. Strnadova, J. Park, B. J. Cummings, A. J. Anderson, L. D. Shea, *Acta Biomater.* **2019**, *86*, 312.
[18] E. Sideris, S. Kioulaphides, K. L. Wilson, A. Yu, J. Chen, S. T. Carmichael, T. Segura, *Adv. Ther.* **2022**, *5*, https://doi.org/10.1002/adtp.202200048.
[19] D. R. Griffin, W. M. Weaver, P. O. Scumpia, D. Di Carlo, T. Segura, *Nat. Mater.* **2015**, *14*, 737.
[20] Y. Liu, A. Suarez-Arnedo, L. Riley, T. Miley, J. Xia, T. Segura, *Adv. Healthcare Mater.* **2023**, e2300823.
[21] J. M. Lowen, G. C. Bond, K. H. Griffin, N. K. Shimamoto, V. L. Thai, J. K. Leach, *Adv. Healthcare Mater.* **2023**, e2202239.
[22] C. M. Walsh, J. K. Wychowaniec, D. F. Brougham, D. Dooley, *Pharmacol. Ther.* **2022**, *234*, 108043.
[23] A. M. Thomas, M. B. Kubilius, S. J. Holland, S. K. Seidlits, R. M. Boehler, A. J. Anderson, B. J. Cummings, L. D. Shea, *Biomaterials* **2013**, *34*, 2213.
[24] D. M. Basso, L. C. Fisher, A. . Anderson, L. B. Jakeman, D. M. Mctigue, P. G. Popovich, *J. Neurotrama.* **2006**, *23*, 635.
[25] B. J. Cummings, C. EngesserCesar, A. J. Anderson, *Behav Brain Res.* **2007**, *177*, 232
[26] A. Shikanov, R. M. Smith, M. Xu, T. K. Woodruff, L. D. Shea, *Biomaterials* **2011**, *32*, 2524.
[27] R N. Kent, M. Said, M E. Busch, E R. Poupard, A. Tsai, J. Xia, D L. Matera, W Y. Wang, S J. DePalma, H L. Hiraki, M L. Killian, A C. Abraham, J.-W. Shin, A H. Huang, A. Shikanov, B M. Baker, *Adv. Funct. Mater.* **2022**, *32*, 2207556.
[28] A. Sheikhi, D. Di Lisa, J. De Rutte, O. Akouissi, D. Di Carlo, A. Khademhosseini, *ACS Appl Polym Mater* **2019**, *1*, 1935.
[29] T. H. Qazi, V. G. Muir, J. A. Burdick, *ACS Biomater. Sci. Eng.* **2022**, *8*, 1427.
[30] N. J. Darling, W. Xi, E. Sideris, A. R. Anderson, C. Pong, S. T. Carmichael, T. Segura, *Adv. Healthcare Mater.* **2020**, *9*, 1901391.
[31] A. Karimi, A. Shojaei, P. Tehrani, *J Chem Neuroanat* **2017**, *86*, 15.
[32] J. Yu, N. Manouchehri, S. Yamamoto, B. K. Kwon, T. R. Oxland, *J. Mech. Behav. Biomed. Mater.* **2020**, *112*, 104044.
[33] H. Ozawa, T. Matsumoto, T. Ohashi, M. Sato, S. Kokubun, *J. Neurosurg* **2001**, *95*, 221.
[34] D. B. Emiroglu, A. Bekcic, D. Dranseikiene, X. Zhang, T. Zambelli, A. J. Demello, M. W. Tibbitt, *Sci Adv.* **2022**, *8*, 50.
[35] D. Librianto, I. S Fachrisal, *Int. J. Surg. Case Rep.* **2020**, *75*, 497.
[36] J. H. Herndon, C. G Hermes, E. J. Riseborough, J. C. Rich, *Arch. Surg.* **1972**, *104*, 107.
[37] J. Park, Y. Zhang, E. Saito, S. J. Gurczynski, B. B. Moore, B. J. Cummings, A. J. Anderson, L. D. Shea, *Proc. Natl. Acad. Sci. USA* **2019**, *116*, 14947.
[38] T. Yang, Y. J. Dai, G. Chen, S. Sen Cui, *Front. Cell Neurosci.* **2020**, *14*, 78.
[39] Y. Zhu, C. Soderblom, M. Trojanowsky, D. H. Lee, J. K. Lee, *J Neurotrauma* **2015**, *32*, 1158.
[40] N. D'Ambrosi, S. Apolloni, *Front Immunol* **2020**, *11*, 1394.
[41] H. X. Nguyen, K. D. Beck, A. J. Anderson, *J Vis Exp* **2011**, *50*, 2698.
[42] L. M. Milich, C. B. Ryan, J. K. Lee, *Acta Neuropathol.* **2019**, *137*, 785.
[43] J. Park, J. T. Decker, D. J. Margul, D. R. Smith, B. J. Cummings, A. J. Anderson, L. D. Shea, *Mol. Ther.* **2018**, *26*, 1756.
[44] O. Bin-Alamer, L. S. Bhenderu, C. Stuebe, N. S. Sagoo, P. Palmisciano, M. Haider, S. G. Aoun, A. S. Haider, *Spinal Cord* **2022**, *60*, 845.

[45] C. Soderblom, X. Luo, E. Blumenthal, E. Bray, K. Lyapichev, J. Ramos, V. Krishnan, C. Lai-Hsu, K K. Park, P. Tsoulfas, J K. Lee, *J. Neurosci.* **2013**, *33*, 13882.
[46] J. Fang, J. Koh, Q. Fang, H. Qiu, M M. Archang, M. M. Hasani-Sadrabadi, H. Miwa, X. Zhong, R. Sievers, D.-W. Gao, R. Lee, D. Di Carlo, S. Li, *Adv. Funct. Mater.* **2020**, *30*, https://doi.org/10.1002/adfm.202004307.
[47] Y. M. Yuan, C. He, *Neurosci. Bull* **2013**, *29*, 421.
[48] L. R. Nih, E. Sideris, S. T. Carmichael, T. Segura, *Adv. Mater.* **2017**, *29*, 1606471.
[49] H. Wang, G. Song, H. Chuang, C. Chiu, A. Abdelmaksoud, Y. Ye, L. Zhao, *Int J Immunopathol Pharmacol* **2018**, *31*, 1.
[50] T. Tjoa, H. J. Strausbaugh, N. Maida, P. F. Dazin, S. D. Rosen, L. J. Noble-Haeusslein, *J Neurosci Methods* **2003**, *129*, 49.
[51] V. Neirinckx, C. Coste, R. Franzen, A. Gothot, B. Rogister, S. Wislet, *J. Neuroinflammation* **2014**, *11*, 150.
[52] A. R. Sas, K. S. Carbajal, A. D. Jerome, R. Menon, C. Yoon, A. L. Kalinski, R. J. Giger, B. M. Segal, *Nat. Immunol.* **2020**, *21*, 1496.
[53] N. R. Chan, B. Hwang, B. D. Ratner, J. D. Bryers, *J Tissue Eng. Regen. Med.* **2022**, *16*, 297.
[54] K. A. Kigerl, J. C. Gensel, D. P. Ankeny, J. K. Alexander, D. J. Donnelly, P. G. Popovich, *J. Neurosci.* **2009**, *29*, 13435.
[55] C. D. Thompson, J. C. Zurko, B. F. Hanna, D. J. Hellenbrand, A. Hanna, *J Neurotrauma* **2013**, *30*, 1311.
[56] B. Zheng, M. H. Tuszynski, *Nat. Rev. Mol. Cell Biol.* **2023**, *24*, 396.
[57] E. J. Bradbury, E. R. Burnside, *Nat. Commun.* **2019**, *10*, 3879.
[58] M A. Anderson, T M. O'Shea, J E. Burda, Y. Ao, S L. Barlatey, A M. Bernstein, J H. Kim, N D. James, A. Rogers, B. Kato, A L. Wollenberg, R. Kawaguchi, G. Coppola, C. Wang, T J. Deming, Z. He, G. Courtine, M V. Sofroniew, *Nature* **2018**, *561*, 396.
[59] M. Ueno, T. Yamashita, *Biologics* **2008**, *2*, 253.
[60] R. G. Fessler, R. Ehsanian, C. Y. Liu, G. K. Steinberg, L. Jones, J. S. Lebkowski, E. D. Wirth, S. L. McKenna, *J. Neurosurg. Spine* **2022**, *37*, 812.
[61] N. Li, G. K. K. Leung, *Biomed. Res. Int.* **2015**, *2015*, 235195.
[62] A. Muheremu, L. Shu, J. Liang, A. Aili, K. Jiang, *Transl. Neurosci.* **2021**, *12*, 494.
[63] R. M. Dorrian, C. F. Berryman, A. Lauto, A. V. Leonard, *Front. Cell Neurosci.* **2023**, *17*, 1095259.
[64] D. R. Stirling, M. J. Swain-Bowden, A. M. Lucas, A. E. Carpenter, B. A. Cimini, A. Goodman, *BMC Bioinformatics* **2021**, *22*, 433.
[65] J. Schindelin, I. Arganda-Carreras, E. Frise, V. Kaynig, M. Longair, T. Pietzsch, S. Preibisch, C. Rueden, S. Saalfeld, B. Schmid, J.-Y. Tinevez, D. J. White, V. Hartenstein, K. Eliceiri, P. Tomancak, A. Cardona, *Nat. Methods* **2012**, *9*, 676.
[66] S. Berg, D. Kutra, T. Kroeger, C N. Straehle, B X. Kausler, C. Haubold, M. Schiegg, J. Ales, T. Beier, M. Rudy, K. Eren, J. I. Cervantes, B. Xu, F. Beuttenmueller, A. Wolny, C. Zhang, U. Koethe, F A. Hamprecht, A. Kreshuk, *Nat. Methods* **2019**, *16*, 1226.
[67] D A. McCreedy, D J. Margul, S K. Seidlits, J T. Antane, R J. Thomas, G M. Sissman, R M. Boehler, D R. Smith, S W. Goldsmith, T V. Kukushliev, J B. Lamano, B H. Vedia, T. He, L D. Shea, *J Neurosci Methods* **2016**, *263*, 15.